Electrical conduction mechanisms in graphene nanoplatelet/yttria tetragonal zirconia composites

R. Poyato[1,2], J. Osuna[2], A. Morales-Rodríguez[2], Á. Gallardo-López[2].

1. Inst. Ciencia de Materiales de Sevilla, ICMS, CSIC-Universidad de Sevilla. Américo Vespucio 49. 41092 Sevilla. Spain.

2. Dpto. de Física de la Materia Condensada. ICMS, CSIC-Universidad de Sevilla. Apdo. 1065. 1080 Sevilla. Spain.

Abstract

Yttria tetragonal zirconia polycrystalline (3YTZP) ceramic composites with 5, 10 and 20 vol% graphene nanoplatelets (GNPs) were prepared by spark plasma sintering (SPS) and their electrical conductivity as a function of temperature was characterized. The composites exhibit anisotropic microstructures so the electrical conductivity studies were carried out in two directions: perpendicular ($\sigma_\perp$) and parallel ($\sigma_\parallel$) to the SPS pressing axis. The composites with 5 and 10 GNP vol% showed high electrical anisotropy, whereas the composite with 20 GNP vol% exhibited nearly isotropic electrical behavior. $\sigma_\perp$ shows metallic-type behavior in the composites with 10 and 20 vol% GNP revealing that charge transport takes place through defect-free GNPs. For the composite with 5 vol% GNP the observed semiconductor-type behavior was explained by a two dimensional variable range hopping mechanism. $\sigma_\parallel$ shows metallic-type conductivity in the composite with 20 GNP vol% and positive $d\sigma_\parallel/dT$ slope in the composites with 5 and 10 GNP vol%.

1. Introduction.

During the last few years, the incorporation of carbon nanostructures, as carbon nanotubes or graphene nanoplatelets into ceramic matrices in order to achieve an enhanced electrical conductivity has awakened a great interest [1-11]. Turning structural ceramics into electrically conductive materials by incorporation of a filler would allow the implementation of these materials in applications such as micro-electro-mechanical systems (MEMS), as it makes possible the manufacturing of miniaturized complex shapes

by using the electro-discharge machining (EDM) technique [2]. Structural ceramics are usually hard to machine using the conventional manufacturing tools due to their high hardness and brittle nature. Thus, achieving the high electrical conductivity that is required for the application of this technique, and the EDM performance of these composites are very interesting issues that have been approached in different studies [2,12-14].

Carbon nanotubes and monolayer graphene are well known for their exceptional electrical conductivity, with extremely high electron mobility at room temperature [15,16]. However, graphene-based nanomaterials as few layer graphene (FLG), multilayer graphene (MLG), or graphene nanoplatelets (GNPs, also called graphite nanoplatelets) have recently appeared into the scene as less expensive alternatives and also exhibiting remarkable electrical properties [17]. These nanomaterials are formed by the stacking of graphene sheets, that range from 2 to 5 layers for FLG, less than 10 layers for MLG, and more than 10 layers for GNPs (in this case they should have a thickness below 100 nm). They also differ in the average lateral size and the carbon-to-oxygen atomic ratio [18,19]. The incorporation of GNPs as a second phase in ceramicmatrix composites appears as a cost-effective alternative resulting in high performance materials with enhanced electrical properties [1,4-6,8,10,20,21].

Together with the achievement of a high electrical conductivity in the GNP/ceramic composites, it is very important to attain a fundamental knowledge of the conduction mechanisms responsible for the electrical response in these materials. To this end, it is essential to be aware of the electrical transport properties of graphene and graphenebased nanomaterials and how they are modified by the presence of defects or other factors.

Although quasi-ballistic type conductivity has been reported for highly crystallized defect-free graphene, conventional metallic behaviour, with an increase of resistance with temperature has been reported for suspended graphene and graphene deposited on a substrate [22]. This metallic-type behavior is similar to the one known for single crystal graphite or highly oriented pyrolytic graphite (HOPG) [23,24]. However, the presence of defects in HOPG results in a modification of the conduction type, turning from a metallic behavior to a semiconductor one, in which conductivity increases with rising temperature. The same effect was observed for highly disordered graphene such as chemically derived graphene monolayers or graphene grown by chemical vapor deposition (CVD) using Ni as a catalyst.

In these cases, the electrical behavior was modelled considering a structure where highly disordered regions are penetrated by percolating metal-like conduction paths. A thermally-assisted two-dimensional variable-range hopping (2D-VRH) conduction model through disordered regions was proposed [22,25,26], and the electrical conductivity was described by:

$$\sigma = \sigma_0 \exp\left(-BT^{-1/3}\right) \quad (1)$$

where σ_0 is a pre-exponential factor and B is a hopping parameter that assesses the energy cost associated to the average charge hopping needed to overcome the disordered regions through the graphene monolayer.

The studies about the electrical transport properties of multilayer graphene or graphene nanoplatelets are still scarce. However, a significant effect of defects on the conduction mechanisms has been clearly shown. Thiyagarajan et al [27] studied multilayer graphene obtained from HOPG *via* mechanical exfoliation and transferred to a SiO_2/Si substrate, with thickness ~21 and ~35 nm. These authors showed that in defect-free MLG, current flows across the graphene channel in the main *ab*-plane with metallic-type behavior, while *c*-axis charge transport is not significant. However, after inducing defects by irradiation with Ar plasma, *c*-axis conduction becomes more significant due to the presence of nanoholes in the MLG, and the material exhibits a semiconductor-like temperature dependence of the electrical resistivity. Gross et al [28] obtained oxidized-graphenic nanoplatelets (OGNP) using bamboo pyroligneous acid as a source, with thickness ranging between 25 and 60 nm and different oxygen contents and sp^2/sp^3 hybridization ratios. For the nanoplatelets synthesized at the highest carbonization temperature, they found that the oxygen content was reduced to 5% and the structure was mainly in sp^2 bonding configuration (sp^2 fraction of 87%). Nevertheless, the conductivity temperature dependence showed typical semiconductor behavior, and was described by the Mott three-dimensional VRH mechanism (3D-VRH) [28].

To the best of our knowledge, only two studies approaching the analysis of the electric transport properties in GNP/ceramic composites can be found in literature. The electrical conductivity as a function of temperature in composites with Si_3N_4 [4] and SiC [6] matrices and GNPs as filler was studied in two different configurations: in the direction perpendicular to the pressing axis during sintering, and in the direction parallel to this axis. Different conduction mechanisms were apparent for the two orthogonal orientations and they were related to the microstructural features in each case. The charge transport along the GNP *ab*-

plane was explained by the 2D-VRH model, assuming that the GNPs behave in a similar way as chemically derived graphene monolayers.

In recent years, the study of composites with yttria stabilized zirconia matrix and graphene nanoplatelets has emerged as an interesting research topic [10,20,21,29-33], given that this ceramic is a technologically significant material used in many structural and biomedical applications and it is expected that its performance will be enhanced by the incorporation of GNPs. Recent studies have mainly focused on the microstructural and mechanical characterization of the composites, revealing an enhancement of properties such as hardness and fracture toughness for GNP contents up to 3 wt% [29-33]. Despite the promising values of electrical conductivity obtained for these composites [20,21], the published works including electrical characterization are still scarce and none of them deals with the analysis of the transport mechanisms.

This study is devoted to the understanding of the electrical conduction mechanisms in GNP/3YTZP composites. To this aim, composites with 5, 10 and 20 GNP vol% nominal contents were prepared by SPS. The microstructure was characterized by SEM and Raman spectroscopy. Electrical conductivity studies as a function of temperature were carried out in the directions perpendicular and parallel to the SPS pressing axis.

The electrical transport properties in each configuration were modeled and related to the microstructure of each composite.

2. Experimental procedure.

2.1. Composites fabrication.

The composites were prepared following a procedure described in a previous work [10].

Briefly, a dispersion of the GNPs (≤ 5 μm planar diameter and 50–100 nm thickness, Angstron Materials, Dayton, Ohio, USA) in isopropyl alcohol was subjected to ultrasonic agitation for 15 min by means of a ultrasonic probe (Model KT-600, Kontes Inc., Vineland, NJ, USA) at 20 kHz and 95% amplitude, in time intervals of 5 min to avoid heating of the suspension to over 30 °C. The 3YTZP powder (40 nm particle size, Tosoh Corporation, Tokyo, Japan) was added to the GNP suspension and sonicated for 5 min in order to homogenize the mixture. After drying on a hot plate with continuous magnetic stirring, the composite powders were homogenized in an agatha mortar and sintered by SPS (Model

515S, SPS Dr Sinter Inc., Kanagawa, Japan) at 1250 ºC for 5 min with an applied uniaxial pressure of 75 MPa. The temperature was measured by means of an optical pyrometer focused on the side of the graphite die. In this way, composites with 5, 10 and 20 vol% GNPs were fabricated. The sintered composites of ~15 mm in diameter and ~2 mm in thickness were manually ground to eliminate the surface graphite from the SPS moulding system.

2.2. Characterization of the starting powders and the sintered composites.

During the wet powder processing, in the different steps there is a possibility of GNP or ceramic powder losses (adhered to the sonication tip or to the different containers), so the real GNP content could be different than the nominal one. In order to account for this variations, elemental microanalysis (Elemental Analyzer TruSpec micro LECO) was performed to evaluate the total C content (and consequently, the GNP content) in the composite powders prior to sintering. Approximately 1–3 mg of the composite powder were placed in Sn capsules and completely burned in a pure oxygen environment at temperatures between 100 and 1000 °C. The combustion product (CO_2) was quantified by an infrared cell.

The density of the sintered composites was measured by the Archimedes method using distilled water as immersion medium. The theoretical density of the composites was calculated using the rule of the mixtures, considering $\rho = 6.1$ g cm^{-3} for 3YTZP and $\rho = 2.2$ g cm^{-3} for the GNPs (data from the suppliers). The GNP volume fractions obtained from the elemental microanalysis were used.

The Raman spectra of the fracture surfaces of the sintered composites were obtained using a dispersive microscope (Horiba Jobin Yvon LabRam HR800, Kyoto, Japan) equipped with a He-Ne green laser (532.14 nm) at 20 mW power as the source. The microscope used a 100x objective and a confocal pinhole of 100 μm. The Raman spectrometer was calibrated using a silicon wafer. Six to eight spectra were taken for each sample.

Microstructural observations of the sintered composites were carried out on polished surfaces by scanning electron microscopy (SEM, FEI-Teneo microscope, FEI, USA) with the aim to assess the GNP distribution in the 3YTZP matrix. Cross-section (c.s.) and in-plane (i.p.) slices, i.e. surfaces parallel and perpendicular to the SPS pressing direction, were

polished with diamond paste up to 1 μm for morphological studies, in order to account for any degree of anisotropy.

Electrical characterization was carried out by impedance spectroscopy using an Agilent 4294A analyzer in the frequency range 100 Hz - 2 MHz. In order to collect data in a temperature range from 25 to 450 ºC, the samples were placed in an alumina tubular furnace. The electrical measurements were carried out in argon atmosphere to avoid oxidation of the samples and subsequent degradation of the GNPs during the process.

Two different electrode configurations were used with the aim to acquire electrical conductivity in the directions parallel ($\sigma_{\parallel}$) and perpendicular ($\sigma_{\perp}$) to the SPS pressing axis, in order to account for any degree of electrical anisotropy. Colloidal silver paste was applied on both sides of the samples and electrodes were fired at 600 ºC for 30 min under argon flow.

3. Results and discussion.

3.1. Composition and microstructure.

Fully dense composites were obtained for the three GNP contents (Table 1). The relative densities were calculated using the real GNP vol% obtained from the elemental microanalysis study. There were only small losses of GNP or 3YTZP powder during the composite powder processing (Table 1). The GNP content is ~0.5 vol% lower than the nominal one for composites with 5 and 10 vol% GNP (due to GNP losses during processing) and the GNP content is ~3 vol% higher than the nominal one for the composite with 20 vol% GNP (due to 3YTZP powder losses during processing). The relative densities obtained in this study reveal the adequacy of the selected SPS conditions for sintering this type of composites, and are higher than reported values for GNP/3YTZP composites with lower GNP contents and SPSed at higher temperatures [29,32]. Also, these authors reported a decrease in relative density when increasing GNP content.

Low-magnification scanning electron micrographs obtained using backscattered electrons illustrate the GNP distribution into the ceramic matrix in the polished i.p. and c.s. surfaces of the composites (Fig. 1). The light and dark phases observed in the micrographs correspond to the 3YTZP matrix and the GNPs, respectively. Both phases can be clearly differentiated because of the high contrast due to the average atomic number difference

between them. The GNPs appear well distributed along the ceramic matrix, and some groups of interconnected or piled up GNPs can also be observed. A higher presence of the dark phase is observed in the micrographs when increasing the GNP content, revealing better percolating networks.

In the composites with 5 and 10 GNP vol%, while the GNPs present a random orientation on the i.p. surface (Fig. 1a and 1c), a preferential alignment is clearly observed from micrographs on the c.s. plane (Fig. 1b and 1d), with their *ab*-plane disposed perpendicular to the direction of applied pressure during sintering. A more remarkable alignment is observed in the composite with 10 GNP vol% (Fig. 1d). This structural anisotropy has been previously shown for composites with different ceramic matrices sintered under uniaxial pressure conditions [4,6,8,9,34,35]. The uniaxial load applied during sintering and the high aspect ratio and stiffness of the GNPs have been pointed out as the key factors for this preferential alignment.

The BSE images corresponding to the i.p. and c.s. surfaces of the composite with 20 GNP vol% (Fig. 1e and 1f) also show microstructural anisotropy in this composite. However, in this case the GNPs are distributed surrounding GNP-free ceramic areas, which show a rounded shape (~40 μm diameter) on the i.p. surface (Fig. 1e) and an oval one with the largest axis (~30-100 μm) in the direction perpendicular to the SPS compression axis on the c.s. surface (Fig. 1f). The existence of GNP-free ceramic areas is consequence of the formation of ceramic powder clusters without GNP incorporation in the composite powders before sintering. These spherical clusters are distorted by the pressure applied during sintering giving place to the oval areas observed in the c.s. surface.

Despite the described arrangement of the GNPs in the matrix, with a preferential alignment in the direction perpendicular to the SPS pressing axis, in all the composites some GNPs with their *ab*-plane disposed in the direction parallel to the SPS pressing axis, that is, disposed in a perpendicular way with respect to most of the GNPs, can be found (see detail for the composite with 5 GNP vol% in Fig. 1g).

The Raman spectra acquired on the fracture surfaces of the studied composites are shown in Figure 2. The characteristic bands for graphene nanoplatelets, D, G and 2D, are observed for the three composites, being located at the same positions in all the spectra. The shape of the spectra, together with the observed I_G/I_{2D} ratios ($I_G > I_{2D}$), confirm the multilayered

character of the nanoplatelets, as it has been shown that for graphene-based structures (multilayer graphene, graphene nanosheets, GNPs, ...) with more than 10 layers the Raman spectra resembles the corresponding one for bulk graphite [36].

The presence of the characteristic bands and the relatively low I_D/I_G ratios (included in Fig. 2) confirm the structural integrity of the GNPs after the powder processing and sintering. The D-band is considered a disorder-induced band in graphitic materials, and high I_D/I_G values are associated to crystal disorder or defects in these materials [37]. Thus, the low values obtained in the present study and the small increase with respect to the value corresponding to the GNPs before composite processing [10] reveal that, although some structural defects could have been introduced during processing and sintering, significant damage to the GNPs in the composites has not taken place.

3.2. Room temperature electrical conductivity.

Table 1 presents the conductivity data measured at room temperature in the two different electrode configurations, $\sigma_\perp$ and $\sigma_\parallel$. It can be observed that the composites with 5 and 10 vol% GNP present significant electrical anisotropy with $\sigma_\perp > \sigma_\parallel$, as previously reported by other authors for composites with different ceramic matrix [4,6,8,9]. This fact has been related to the preferential alignment of the GNPs in the direction perpendicular to the SPS pressing axis, and to the intrinsic electrical anisotropy in graphene and graphene-related materials. The electrical anisotropy factor is more remarkable in the composite with 10 vol% GNP ($\sigma_\perp/\sigma_\parallel = 6.84 \pm 0.11$) in comparison with the corresponding one for the composite with 5 vol% GNP ($\sigma_\perp/\sigma_\parallel = 3.36 \pm 0.05$) as a consequence of the interconnections between the GNPs in the *ab*-plane that are taking place when increasing the GNP content from 5 to 10 vol%. A much higher conductivity in the *ab*-plane in comparison with the one along the *c*-axis has been reported for different graphitic materials as graphite single crystals [23], HOPG [24,38,39] or nano-laminates [40]. These differences in conductivity, together with the alignment of the GNPs (Fig. 1d) promote the significant enhancement in $\sigma_\perp$ while the increase is just slight for $\sigma_\parallel$ in this composite. However, the electrical anisotropy factors reported here are not as high as the ones reported by previous authors for GNP/Si_3N_4 composites, with $\sigma_\perp/\sigma_\parallel$ ratios in the range 10-25 [4]. This difference could be due to several effects, as the different matrix with different microstructure (the ceramic grains in Si_3N_4 are more elongated than those of 3YTZP) or the different GNP characteristics.

Also, the lower electrical anisotropy factors here reflect that the preferential alignment of the GNPs in the composites under study is not as remarkable as the one achieved in the mentioned GNP/Si3N4 composites.

When the GNP content increases up to 20 vol%, a significant increase of both $\sigma_{\perp}$ and $\sigma_{\parallel}$ is found (Figure 3). However, in this case the most remarkable conductivity enhancement is observed for $\sigma_{\parallel}$, promoting even the decrease of the anisotropy factor to a value of 1.18 ± 0.05. Thus, this composite is almost an electrically isotropic material.

The electrical performance of this composite is clearly related to its microstructure (Fig. 1e and 1f), formed by GNPs surrounding oval GNP-free ceramic areas. In contrast with the composites with lower GNP content, the GNP-free oval regions are much better defined because the GNPs surrounding them are much better interconnected (they present a higher degree of interconnection). The presence of GNPs aligned in different directions other than perpendicular to the SPS pressing axis is much higher in this composite, so the GNPs situated in the direction parallel to the SPS pressing axis greatly contribute with their *ab*-plane to $\sigma_{\parallel}$.

The highest conductivity value achieved in this work (~276 $S \cdot m^{-1}$) is not as high as the reported ones for ceramic composites with similar GNP contents. Conductivities of 1000, 4100 and 4378 $S \cdot m^{-1}$ were reported for Al_2O_3/15 GNP vol% [13], Si_3N_4/24 GNP vol% [4] and SiC/20 GNP vol% [6] composites, respectively. Also, it is similar to the reported value for yttria stabilized zirconia composites with much lower GNP contents (280 $S \cdot m^{-1}$ for composites with 5.5 GNP vol%) [21]. This could be related to the different size and type of GNPs used in the different studies, as it has been reported that the GNP electrical conductivity is highly dependent on the number of graphene layers forming the nanoplatelet. Nanoscale mappings [41] and numerical simulations [42] have shown that the electrical conductivity of few-layer graphene and graphene nanoplatelets decreases with increasing thickness. The conductivity rapidly decreases for thicknesses from 0.67 to 4.4 nm, then slowly decreases from 4.4 to 55-100 nm, and remains constant for higher thicknesses, ultimately approaching that of bulk graphite [42].

Whereas graphene nanoplatelets with thickness ranging from 1 to 10-20 nm were used in the mentioned studies [4,6,13,21], nanoplatelets with 50-100 nm thickness and thus, with lower electrical conductivity, were used in the present study, and consequently, the

electrical conductivity of the composite would be lower. Moreover, as revealed in the microstructural analysis, the GNPs in the composite with 20 vol% are not preferentially aligned in such a remarkably way as they are in the composites reported in literature [4,6].

3.3. Dependence of the electrical conductivity with temperature.

The analysis of the temperature dependence of the conductivity is essential in order to understand the conduction mechanisms in these materials. Fig. 4 shows the experimental conductivity data as a function of temperature. The conductivity values have been plotted versus $T^{-1/3}$ according to the 2D-VRH model (Eq. (1)). This type of thermally-assisted conduction through disordered regions has been successfully applied to describe the electrical transport in GNP/Si3N4 and GNP/SiC composites [4,6]. However, as it will be presented below, this model does not describe properly the behaviour of the more conductive composites of our study.

When analysing the conductivity measured in the direction perpendicular to the SPS pressing axis ($\sigma_{\perp}$) it is observed that only the composite with 5 GNP vol% presents a semiconductor-type behavior, whereas the composites with higher GNP contents show a metallic-type behavior (Fig. 4a). Thus, the 2D-VRH model only describes properly the composite with the lowest GNP content. Taking into account the preferential alignment of the GNPs (Fig. 1) it is clear that when measuring in this direction the charge transport will take place along the *ab*-plane of the aligned GNP. The metallic-type behavior is strongly revealing that the charge transport is taking place through defect-free GNPs in a well percolated network in the composites with 10 and 20 GNP vol%. This makes sense as the commercial GNPs used in this study were not chemically derived from GO layers, and thus, are formed by pristine graphene layers. When the GNP content is lower, the interconnection between nanoplatelets is not as good as for 10 or 20 GNP vol%. The insulating ceramic areas situated between the GNPs can be considered as defects embedded in regions with metallic conduction and the conduction would take place via the variable range hopping of the carriers between the GNPs. The hopping parameter obtained for these 3YTZP composites ($B = 5.75 \pm 0.03\ K^{-1/3}$) is lower than the reported one for GNP/Si_3N_4 composites [4] with GNP content ranging from 11 to 24 vol% (B = 9.5 ± 0.5 K-1/3), suggesting a lower energy cost associated to the charge hopping.

On the other hand, when analysing the conductivity measured in the parallel direction ($\sigma_{||}$) a quite different scenario is found. The composites with 5 and 10 GNP vol%, which show much lower conductivity values, present a semiconductor-type behavior, whereas only the composite with the highest GNP content shows a metallic-type behavior (Fig. 4b). In the latter case, it is worth mentioning again the special microstructure of this composite (Fig. 1e and 1f), with the GNPs closely surrounding GNP-free ceramic areas.

In this configuration, there are also GNPs with the *ab*-plane in the direction parallel to the SPS pressing axis, and thus, taking into account the excellent percolation of the network, metallic-type conduction through the GNPs *ab*-plane takes place also in this direction, for this composite.

The positive $d\sigma/dT$ slope in the composites with the lowest conductivity could be explained in two different ways. On the one hand, a contribution of the *c*-axis conductivity should be considered in the GNPs, as they are formed by a stacking of more than 10 graphene layers, and this contribution has been shown to be semiconductor-type for different types of graphite (single crystal, HOPG, nanolaminate…) [23,38,39,40]. On the other hand, we have shown that despite the preferential alignment of the GNPs in the direction perpendicular to the SPS pressing axis, some GNPs appear disposed with their *ab*-plane in the direction parallel to the SPS pressing (Fig. 2) and could also contribute to $\sigma_{||}$. The hopping parameters obtained for these two composites ($B = 8.4 \pm 0.1\ K^{-1/3}$ and $B = 9.7 \pm 0.2\ K^{-1/3}$ for the composites with 5 and 10 GNP vol%, respectively) are similar to the previously reported one for GNP/Si_3N_4 composites [4].

4. Conclusions.

Fully dense yttria tetragonal zirconia composites with 5, 10 and 20 GNP vol% were fabricated by SPS. Anisotropic microstructures were observed in the composites as a consequence of the uniaxial applied pressure during the sintering process. A preferential alignment of the GNPs was observed in the composites with 5 and 10 GNP vol%, with their *ab*-plane disposed perpendicular to the direction of the applied pressure. A different microstructure, with interconnected GNPs surrounding GNP-free ceramic areas with oval shape was observed in the composite with 20 GNP vol%.

The creation of a higher number of GNP interconnections in the direction perpendicular to the SPS pressing axis when increasing the GNP content from 5 to 10 vol% resulted in a significant increase of the electrical anisotropy factor, $\sigma_{\perp}/\sigma_{\parallel}$. On the contrary, the nearly isotropic electrical behavior in the composite with 20 GNP vol% is consequence of the presence of GNPs aligned in different directions other than perpendicular to the SPS pressing axis in this composite, since the GNPs situated in the direction parallel to this axis greatly contribute with their *ab*-plane to $\sigma_{\parallel}$.

Charge transport through the *ab*-plane in the well percolated defect-free GNPs gives place to a metallic-type behavior of $\sigma_{\perp}$ for the composite with 10 GNP vol% and both $\sigma_{\perp}$ and $\sigma_{\parallel}$ for the composite with 20 GNP vol%. The semiconductor-type behavior for $\sigma_{\perp}$ in the composite with 5 GNP vol% is explained by a two dimensional variable range hopping mechanism between defect-free GNPs. The positive $d\sigma_{\parallel}/dT$ slope in the composites with 5 and 10 GNP vol% has been related to two effects: the contribution of the *c*-axis conductivity and a hopping mechanism between GNPs with their *ab*-plane situated in the parallel direction.

Acknowledgments

The authors acknowledge the financial support provided by the Spanish Ministerio de Economía y Competitividad, under Project MAT2015-67889-P, cofunded by European FEDER funding. Elemental microanalysis and microscopy studies were performed at CITIUS facilities (Universidad de Sevilla).

Figure captions

Figure 1: Backscattered scanning electron (BSE) microscopy images from the composites i.p. (a), (c), (e), and c.s. surfaces (b), (d), (f) for different nominal GNP 10 contents: (a) and (b) 5 vol%, (c) and (d) 10 vol%, (e) and (f) 20 vol%. (g) BSE-SEM image showing a detail from the c.s. surface of the composite with 5 GNP vol%. Compression axis during SPS is indicated in (b) by arrows.

Figure 2: Raman spectra of the 3YTZP composites with 5, 10 and 20 GNP vol%. The I_D/I_G ratios are also indicated. *From Ref. [10].

Figure 3: Electrical conductivity at room temperature as a function of the GNP vol% for both electrode configurations: $\sigma_{\perp}$ (solic circles) and $\sigma_{\parallel}$ (open circles).

Figure 4: Electrical conductivity as a function of temperature for the GNP/3YTZP composites, plotted according to the 2D-VRH model, (a) $\sigma_{\perp}$ and (b) $\sigma_{\parallel}$.

References

1 Y. Fan, L. Wang, J. Li, J. Li, S. Sun, F. Chen, L. Chen, W. Jiang, Preparation and electrical properties of graphene nanosheet/Al2O3 composites, Carbon 48 (2010) 1743– 1749.

2 O. Malek, J. González-Julián, J. Vleugels, W. Vanderauwera, B. Lauwers, M. Belmonte, Carbon nanofillers for machining insulating ceramics, Mater. Today 14 (2011) 496-501.

3 J. González-Julián, Y. Iglesias, A.C. Caballero, M. Belmonte, L. Garzón, C. Ocal, et al, Multi-scale electrical response of silicon nitride/multi-walled carbon nanotubes composites, Comp. Sci. Technol. 71 (2011) 60-66.

4 C. Ramirez, F.M. Figueiredo, P. Miranzo, P. Poza, M.I. Osendi, Graphene nanoplatelet/silicon nitride composites with high electrical conductivity, Carbon 50 (2012) 3607–3615.

5 J.-H. Shin, S.-H. Hong, Fabrication and properties of reduced graphene oxide reinforced yttria-stabilized zirconia composite ceramics, J. Eur. Ceram. Soc. 34 (2014) 1297–1302.

6 B. Román-Manso, E. Domingues, F.M. Figueiredo, M. Belmonte, P. Miranzo, Enhanced electrical conductivity of silicon carbide ceramics by addition of graphene nanoplatelets, J. Eur. Ceram. Soc. 35 (2015) 2723–2731.

7 R. Poyato, J. Macías-Delgado, A. García-Valenzuela, A. Gallardo-López, A. Morales-Rodríguez, A. Muñoz, A. Domínguez-Rodríguez, Mechanical and electrical properties of low SWNT content 3YTZP composites, J. Eur. Ceram. Soc. 35 (2015) 2351-2359.

8 Y. Tan, H. Luo, H. Zhang, S. Peng, Graphene nanoplatelet reinforced boron carbide composites with high electrical and thermal conductivity, J. Eur. Ceram. Soc. 36 (2016) 2679–2687.

9 S. Baskut, A. Cinar, S. Turan, Directional properties and microstructures of spark plasma sintered aluminum nitride containing graphene platelets, J. Eur. Ceram. Soc. 37 (2017) 3759–3772.

10 A. Gallardo-López, I. Márquez-Abril, A. Morales-Rodríguez, A. Muñoz, R. Poyato, Dense graphene nanoplatelet/yttria tetragonal zirconia composites: processing, hardness and electrical conductivity, Ceram. Int. 43 (2017) 11743–11752.

11 P. Miranzo, M. Belmonte, M.I. Osendi, From bulk to cellular structures: A review on ceramic/graphene filler composites, J. Eur. Ceram. Soc. 37 (2017) 3649–3672.

12 D. Hanaoka, Y. Fukuzawa, C. Ramirez, P. Miranzo, M.I. Osendi, M. Belmonte, Electrical discharge machining of ceramic/carbon nanostructure composites, Procedia CIRP 6 (2013) 95–100.

13 J.-W. Sung, K.-H. Kim, M.-C. Kang, Effects of graphene nanoplatelet contents on material and machining properties of GNP-dispersed Al2O3 ceramics for micro-electric discharge machining, Int. J. Precision Eng. Manufacturing-Green Technol. 3 (2016) 247-252.

14 F. Zeller, C. Müller, P. Miranzo, M. Belmonte, Exceptional micromachining performance of silicon carbide ceramics by adding graphene nanoplatelets. J. Eur. Ceram. Soc. 37 (2017) 3813–3821.

15 R.H. Baughman, A.A. Zakhidov, W.A. de Heer, Carbon nanotubes – the route 20 toward applications, Science 297 (2002) 787–792.

16 A.S. Mayorov, R.V. Gorbachev, S.V. Morozov, L. Britnell, R. Jalil, L.A. Ponomarenko, P. Blake, K.S. Novoselov, K. Watanabe, T. Taniguchi, A.K. Geim, Micrometer-scale ballistic transport in encapsulated graphene at room temperature, Nano Lett. 11 (2011) 2396–2399.

17 A. Bianco et al, All in the graphene family – A recommended nomenclature for two-dimensional carbon materials, Carbon 65 (2013) 1–6.

18 B.Z. Jang, A. Zhamu, Processing of nanographene platelets (NGPs) and NGP nanocomposites: a review, J. Mater. Sci. 43 (2008) 5092-5101.

19 P. Wick et al, Classification framework for graphene-based materials, Angew. Chem. Int. Ed. (2014) 7714-7718.

20 S.-M. Kwon, S.-J. Lee, I.-J. Shon, Enhanced properties of nanostructured ZrO2–graphene composites rapidly sintered via high-frequency induction heating, Ceram. Int. 41 (2015) 835–842.

21 K. Markandan, J.K Chin, M.T.T Tan, Enhancing electroconductivity of ytria - stabilised zirconia ceramic using graphene platlets, Key Eng. Mater. 690 (2016) 1-5.

22 A.B. Kaiser, V. Skákalová, Electronic conduction in polymers, carbon nanotubes and

graphene, Chem. Soc. Rev. 40 (2011) 3786–3801.

23 L. Edman, B. Sundqvist, E. McRae, E. Litvin-Staszewska, Electrical resistivity of single-crystal graphite under pressure: an anisotropic three-dimensional semimetal, Phys. Rev. B 57 (1998) 6227-6230.

24 V. Pantin, J. Avila, M.A. Valbuena, P. Esquinazi, M.E. Dávila, M.C. Asensio, Electronic properties of high oriented pyrolitic graphite: recent discoveries, J. Phys. Chem. Solids 67 (2006) 546–551.

25 V. Skákalová, D.S. Lee, T. Beringer, A.B. Kaiser, A. Srivastava, H.J. Park, S. Roth,

Variations of electronic transport in graphene of different origins, Phys. Status Solidi C

26 (2011) 3191–3194.

26 A.B. Kaiser, C. Gómez-Navarro, R.S. Sundaram, M. Burghard, K. Kern, Electrical conduction mechanism in chemically derived graphene monolayers, Nano Lett. 9 (2009) 1787-1792.

27 K. Thiyagarajan, A. Ananth, B. Saravanakumar, Y.S. Mok, S.-J. Kim, Defect-induced metallic-to-semiconducting transition in multilayer grapheme, RSC Adv. 5 (2015) 16821-16827.

28 K. Gross, J.J. Prías Barragán, S. Sangiao, J.M. De Teresa, L. Lajaunie, R. Arenal, H. Ariza Calderón, P. Prieto, Electrical conductivity of oxidized-graphenic nanoplatelets obtained from bamboo: effect of the oxygen content, Nanotechnol. 27 (2016) 365708-365717.

29 F. Chen, D. Jin, K. Tyeb, B. Wang, Y.-H. Han, S. Kim, J.M. Schoenung, Q. Shen, L. Zhang, Field assisted sintering of graphene reinforced zirconia ceramics, Ceram. Int. 41 (2015) 6113–6116.

30 D.-T. Vu, Y.-H. Han, F. Chen, D. Jin, J.M. Schoenung, and D.-Y. Lee, Graphene nano-platelets reinforced ZrO_2 consolidated by spark plasma sintering, Sci. Adv. Mater. 7 (2015) 1–6.

31 J. Liu, H. Guo, Y. Su, L. Wang, L. Wei, G. Yang, Y. Yang, K. Jiang, Spark plasma sintering of graphene platelet reinforced zirconia composites with improved mechanical performance, Mater. Sci. Eng. A 688 (2017) 70–75.

32 S. Li, Z. Xie, Y. Zhang, Y. Zhou, Enhanced toughness of zirconia ceramics with graphene platelets consolidated by spark plasma sintering, Int. J. Appl. Ceram. Technol. 14 (2017) 1062–1068.

33 J. Su, Y. Chen, Q. Huang, Graphene nanosheet-induced toughening of yttria-stabilized zirconia, Appl. Phys. A (2017) 123:10.

34 P. Rutkowski, P. Klimczyk, L. Jaworska, L. Stobierski, D. Zientara, K. Tran, Mechanical properties of pressure sintered alumina-graphene composites, Ceram. Mater. 68 (2016), 168-175.

35 O. Hanzel, R. Sedlák, J. Sedlácek, V. Bizovská, R. Bystrický, V. Girman, A. Kovalcíková, J. Dusza, P. Sajgalík, Anisotropy of functional properties of SiC composites with GNPs, GO and in-situ formed graphene, J. Eur. Ceram. Soc. 37 (2017) 3731–3739.

36 A.C. Ferrari, J.C. Meyer, V. Scardaci, C. Casiraghi, M. Lazzeri, F. Mauri, S. Piscanec, D. Jiang, K.S. Novoselov, S. Roth, A.K. Geim, Raman spectrum of graphene and graphene layers, Phys. Rev. Lett. 97 (18) (2006) 187401.

37 L.M. Malard, M.A. Pimenta, G. Dresselhaus, M.S. Dresselhaus, Raman spectroscopy in graphene, Phys. Reports 473 (2009) 51-87.

38 C. Uher, R.L. Hockey, E. Ben-Jacob, Pressure dependence of the c-axis resistivity of graphite, Phys. Rev. B 35 (1987) 4483- 4488.

39 G. Venugopal, M.-H. Jung, M. Suemitsu, S.-J. Kim, Fabrication of nanoscale dimensional graphite stacked junctions by focused-ion-beam and observation of anomalous transport characteristics, Carbon 49 (2011) 2766–2772.

40 Ł. Zych, P. Rutkowski, L. Stobierski, D. Zientara, K. Mars, W. Piekarczyk, The manufacturing and properties of a nano-laminate derived from graphene powder, Carbon 95 (2015) 809-817.

41 P.N. Nirmalraj, T. Lutz, S. Kumar, G.S. Duesberg, J.J. Boland, Nanoscale mapping of electrical resistivity and connectivity in graphene strips and networks, Nano Lett. 11 (2011) 16–22.

42 X.-Y. Fang, X.-X. Yu, H.-M. Zheng, H.-B. Jin, L. Wang, M.-S. Cao, Temperature and thickness-dependent electrical conductivity of few-layer graphene and graphene nanosheets, Phys. Lett. A 379 (2015) 2245–2251.

Table 1

Table 1: Measured GNP content, density, electrical conductivity and anisotropy ratio for the GNP/3YTZP composites.

GNP vol%	Real GNP vol% ± 0.1	ρ (g/cm^3) ± 0.1	$\rho_{relative}$ (%) ± 2	$\sigma_{\parallel}$ (S·m^{-1})	$\sigma_{\perp}$ (S·m^{-1})	$\sigma_{\perp} / \sigma_{\parallel}$
5	4.4	5.8	99	13.49 ± 0.09	45.3 ± 0.3	3.36 ± 0.05
10	9.5	5.7	100	16.57 ± 0.11	113.3 ± 1.1	6.84 ± 0.11
20	23.4	5.15	100	234 ± 7	275.9 ± 1.9	1.18 ± 0.05

Figure 1

Click here to download high resolution image

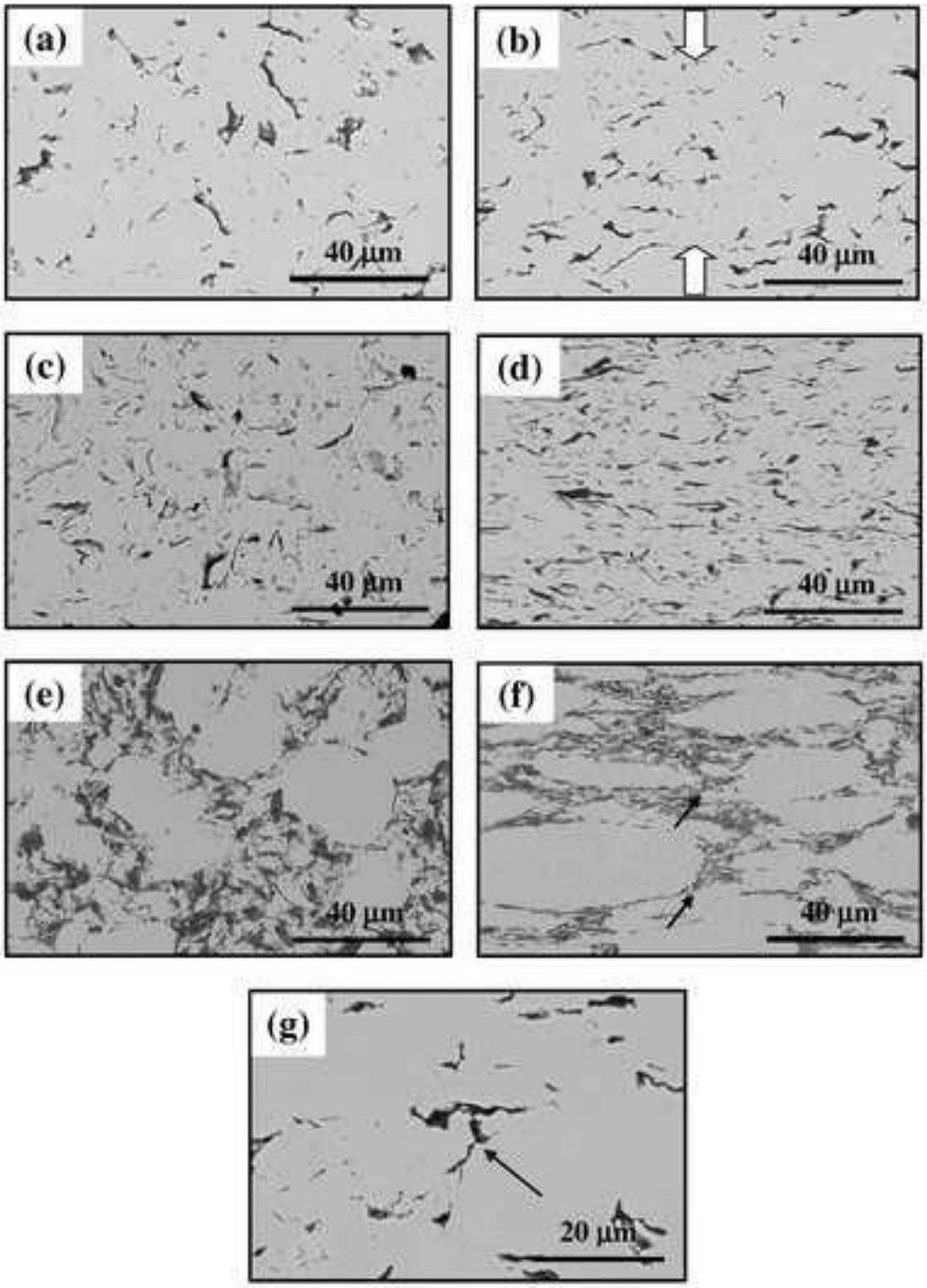

Figure 2

Click here to download high resolution image

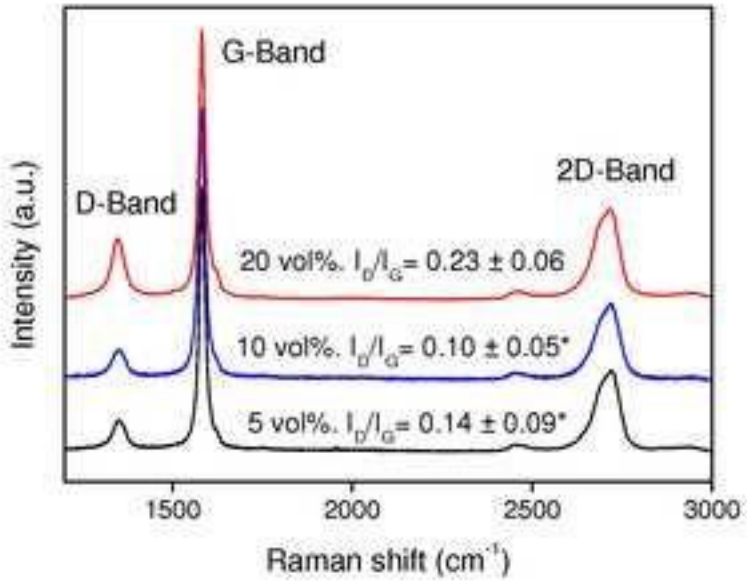

Figure 3

Click here to download high resolution image

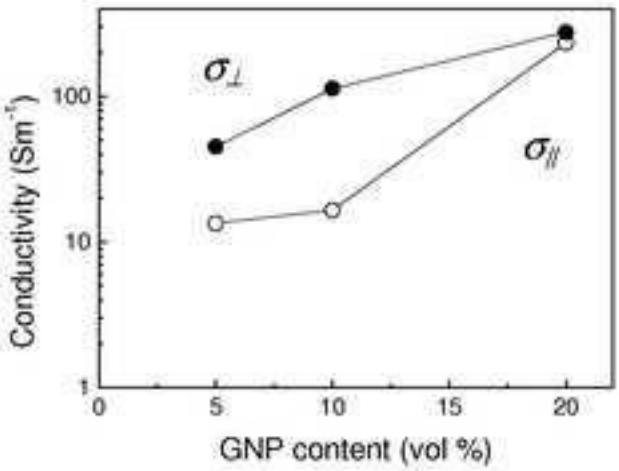

Figure 4

Click here to download high resolution image